Macromolecules

Article

pubs.acs.org/Macromolecules

Photophysical Properties of Partially Functionalized Phenylsilsesquioxane: $[RSiO_{1.5}]_7[Me/nPrSiO_{1.5}]$ and $[RSiO_{1.5}]_7[O_{0.5}SiMe_3]_3$ (R = 4-Me/4-CN-Stilbene). Cage-Centered Magnetic Fields Form under Intense Laser Light

Jun Guan,[†] Kenji Tomobe,[‡] Ifeanyi Madu,[‡] Theodore Goodson, III,[‡,§] Krishnandu Makhal,[⊥] Minh Tuan Trinh,[⊥] Stephen Rand,[∥,⊥] Nuttapon Yodsin,[#] Siriporn Jungsuttiwong,[#] and Richard Laine*[,†,§]

[†]Departments of Materials Science and Engineering, [‡]Chemistry, [§]Macromolecular Science and Engineering, [∥]Applied Physics, and [⊥]Electrical Engineering, University of Michigan, Ann Arbor, Michigan 48109, United States

[#]Department of Chemistry, Ubon Ratchathani University, Ubon Ratchathani, Thailand 34190

Supporting Information

ABSTRACT: Macromonomers $[RPhSiO_{1.5}]_{8,10,12}$ and $[RCH{=}CHSiO_{1.5}]_{8,10,12}$, where R is a conjugated group, have previously been shown to offer photophysical properties wherein excitation promotes an electron from the HOMO to an excited-state LUMO that sits in the center of the cage and allows communication between all conjugated groups, suggesting 3-D delocalization. In the current work, we explore replacing one conjugated group in $[RPhSiO_{1.5}]_8$ with either Me or nPr or simply removing one corner from the cage, $[RPhSiO_{1.5}]_7(O_{0.5}SiMe_3)_3$, and examine its effect on any potential LUMO that might form. We report here that such changes seem to have no effect on the existence of a 3-D LUMO-derived delocalization as witnessed by emission red-shifts from the R = 4-Me-/4-CN-stilbene moieties essentially identical to those for the original $[RPhSiO_{1.5}]_8$ macromonomers. Of particular importance is the fact that removing one corner from the cage also has little effect on the photophysics, indeed significantly improving fluorescence emission quantum efficiencies. However, removing most of the conjugated groups on the corner missing cage (from 7 to 2), e.g., $[MeStilSiO_{1.5}]_2[PhSiO_{1.5}]_5(O_{0.5}SiMe_3)_3$, eliminates the red-shift, implying the absence of a LUMO inside the cage. This suggests a minimum number of groups are needed to form such a LUMO. Also, for the first time, the radiation patterns for nonlinear, optically induced magnetic scattering at elevated light intensities are reported for these compounds and shown to support the same conclusion—a spherical LUMO exists inside the cage.

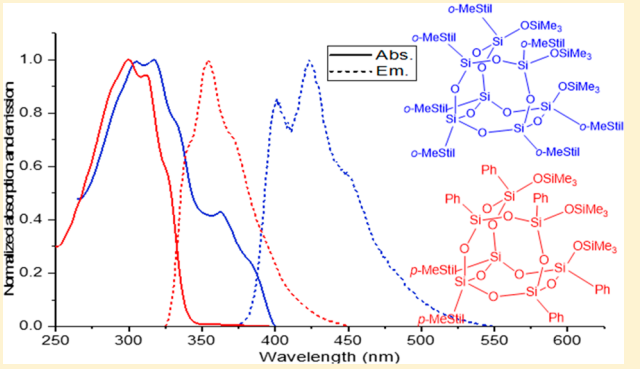

INTRODUCTION

Research on silsesquioxane macromonomers has grown over the past 30 years such that the field has become a major area of chemical exploration with ~17 reviews and one book written in this period.[1−18] As part of our exploration of the chemistries of T_8, T_{10}, and T_{12} cage macromonomers, we have been particularly interested in the chemistries and photophysical properties of the vinyl and phenyl derivatives. This comes from our discovery that they offer properties quite different from what was anticipated to be organic decorated silica. In a series of papers, we determined that these 3-D macromonomers exhibit behavior that reflects the existence of a LUMO within the center of the cage that greatly affects both cage chemistries and photophysical properties.[19−21] They also exhibit unexpected two-photon absorption (TPA) behavior that suggests considerable polarization in the excited state.

In particular, although the cages are recognized to offer electron-withdrawing properties similar to CF_3,[22] the phenyl cages exhibit very different reactivities during electrophilic substitution. For example, traditional Friedel−Crafts acylation, sulfonylation, and nitration do indeed favor formation of meta-substituted products[17] as might be expected. However, bromination and iodination selectivities are quite disparate. For example, the $PhT_{8,10,12}$ cages all iodinate almost exclusively (>90% selectivity) in the para position. In contrast, bromination occurs selectively in the ortho position (85% PhT_8, 70% PhT_{10}, and 60% PhT_{12}). This selectivity is likely defined by the separation between phenyl groups on

Received: April 8, 2019
Revised: May 7, 2019

DOI: 10.1021/acs.macromol.9b00699
Macromolecules XXXX, XXX, XXX−XXX

neighboring positions on the cages. The phenyl groups are 90°, 72°, and 60° apart as the cage size increases limiting access of Br_2 to ortho hydrogens.

Although we have yet to identify a mechanistic pathway whereby iodination occurs selectively in the para position, we have carefully modeled the bromination process. We find that the cage-centered LUMO engages an incoming Br_2 and together with hydrogen bonding to ortho hydrogens leads to formation of an energetically favored transition state akin to a Venus flytrap that selectively drives ortho bromination (Figure 1).[23]

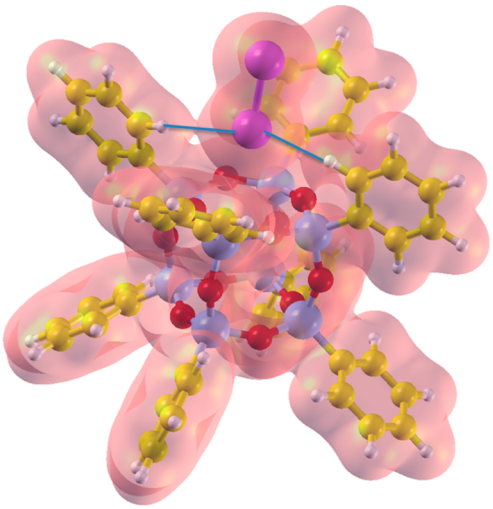

Figure 1. Venus flytrap mechanism for ortho bromination.[23]

More recently, we reported that the first bromine on the cage promotes bromination on the same face of the cage as illustrated in Figures 2 and 3.[24] The crystal structure in Figure 3 shows that careful bromination allows the synthesis and isolation of a Janus brominated cage.[25]

Several other research groups have now isolated related cage macromonomers with cage-centered LUMOs that also lead to unusual properties including a germanium analogue as shown in Figure 4.[26]

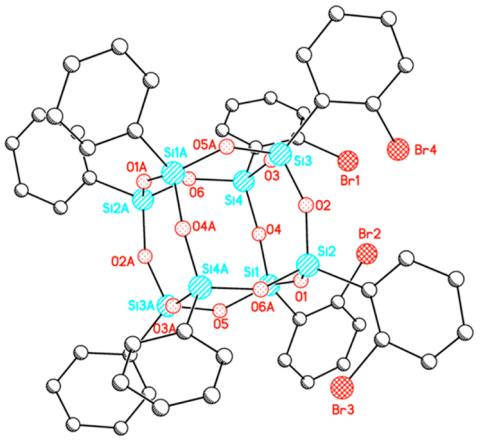

Figure 3. Janus bromination of octaphenylsilsesquioxanes.[25]

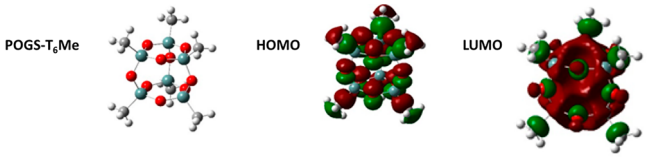

Figure 4. Polyhedral germsesquioxane cage with LUMO centered within the cage.[26]

These recent results suggest that the presence of LUMOs inside such cage macromonomers might be more common than our earlier results suggested. To this end, we decided to systematically study the effects of replacing one phenyl on the cage with a simple alkyl—methyl or *n*-propyl—or simply making a cage missing a corner and exploring the synthesis of model stilbene compounds to test the potential for LUMO formation in the unsymmetrical cages: $MePh_7[SiO_{1.5}]_8$, $PrPh_7[SiO_{1.5}]_8$, and $[PhSiO_{1.5}]_7(O_{0.5}SiMe_3)_3$. We report here the bromination and iodination of these model cages, their conversion to 4-methylstilbene and 4-cyanostilbene derivatives, spectroscopic characterization of the formed products, and their photophysical properties. We find that indeed even with a missing corner a LUMO forms in the cages and yields a form of excited-state delocalization results as reported for the octaphenylsilsesquioxane analogues, except in the case of

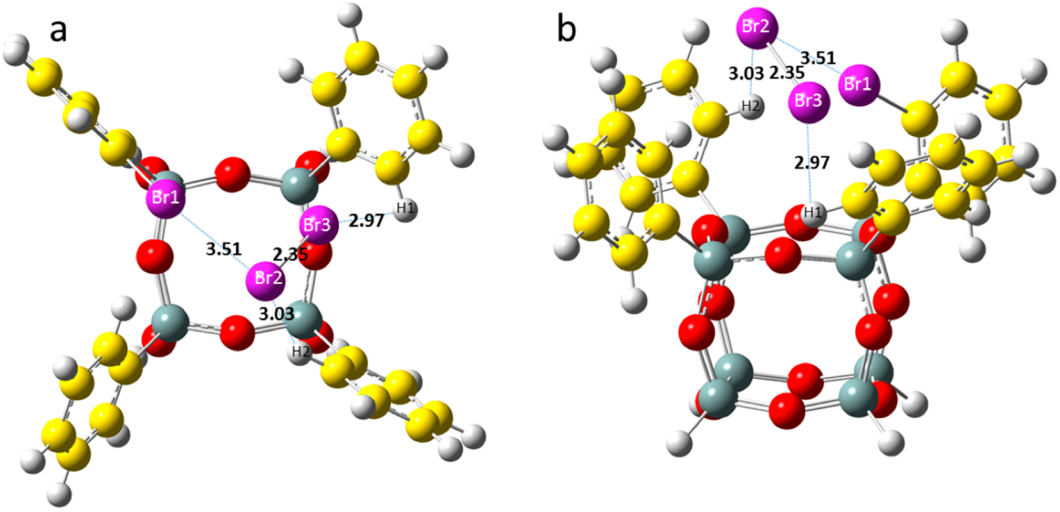

Figure 2. Asymmetric bromination.[24]

DOI: 10.1021/acs.macromol.9b00699
Macromolecules XXXX, XXX, XXX−XXX

$[MeStilSiO_{1.5}]_2[PhSiO_{1.5}]_5(O_{0.5}SiMe_3)_3$.[19−21] We also report for the first time magneto-optic properties that support the existence of spherical LUMOs inside these cages.

EXPERIMENTAL SECTION

Materials. All commercially available chemicals were used as received unless otherwise indicated. Trisilanol corner-missing phenylsilsesquioxane $[PhSiO_{1.5}]_7[O_{0.5}H]_3$ [T_7-triol] was purchased from Hybrid Plastics. Methyltrichlorosilane ($MeSiCl_3$), propyltrichlorosilane ($nPrSiCl_3$), trimethylchlorosilane (Me_3SiCl), triethylamine (Et_3N), tris(dibenzylideneacetone)dipalladium(0) ($Pd_2(dba)_3$), bis(tri-*tert*-butylphosphine)palladium(0) ($Pd(t\text{-}Bu_3P)_2$), *N*,*N*-dicyclohexylmethylamine (NCy_2Me), 4-methylstyrene (C_9H_{10}), and *N*-acetyl-L-cysteine ($HSCH_2CH(NHCOCH_3)CO_2H$) were purchased from Sigma-Aldrich. Bromine, Br_2, and 4-cyanostyrene, and C_9H_7N were purchased from Fisher Scientific. THF was purchased from Fisher Scientific and distilled under nitrogen from Na/benzophenone ketyl prior to use.

Synthesis of Ph_7T_8R' (R′ = Me/nPr).[27] To a dry 250 mL Schlenk flask under N_2 were added Ph_7T_7-triol (10.0 g, 10.75 mmol), 75 mL of THF, and $R'SiCl_3$ (11.83 mmol). Following the addition, a 25 mL of THF solution of Et_3N (4.4 g, 43.0 mmol) was added over a 10 min period. The reaction was stirred magnetically under N_2 for 24 h and then transferred to a separatory funnel. It was washed with brine (10 mL), 1 M HCl (10 mL), and brine (10 mL), and diethyl ether was added to extract the organic layer. Thereafter, the organic layer was dried over $MgSO_4$, and most solvent was removed by rotary evaporation. The resulting thick slurry was slowly poured into cold, well-stirred methanol (100 mL) to fully precipitate the product, which was recovered by filtration and dried under vacuum to give a 75% yield of white product.

Synthesis of Ph_7T_7-Trisiloxy.[27] To a dry 250 mL Schlenk flask under N_2 were added Ph_7T_7-triol (10.0 g, 10.75 mmol), 100 mL of THF, Et_3N (6.5 g, 64.5 mmol), and Me_3SiCl (7.0 g, 64.5 mmol). The reaction was stirred magnetically under N_2 for 24 h and then transferred to a separatory funnel. It was washed with brine (10 mL), 1 M HCl (10 mL), and brine (10 mL), and diethyl ether was added to extract the organic layer. Thereafter, the organic layer was dried over $MgSO_4$, and most solvent was removed by rotary evaporation. The resulting thick slurry was slowly poured into cold, well-stirred methanol (100 mL) to fully precipitate the product, which was recovered by filtration and dried under vacuum to give a 70% yield of white product.

General Bromination of Ph_7T_8R' and Ph_7T_7-Trisiloxy.[28] To a dry 100 mL Schlenk flask under N_2 were added Ph_7T_8R' or Ph_7T_7-trisiloxy (5.0 mmol, phenyl: 35.0 mmol) and 25 mL of CH_2Cl_2. A condenser was then attached, and the flask was heated to 45 °C in an oil bath. Thereafter, Br_2 (3.0 mL, 57.8 mmol) was added dropwise to the solution, and an additional 3 mL of CH_2Cl_2 was added to wash the condenser. After that, a vent to a bubbler containing aqueous base was added, and the solution was stirred magnetically under reflux at 45 °C for 5.5 h. At this point, 20 g of $Na_2S_2O_5$ and 10 g of Na_2CO_3 were dissolved in 40 mL of water and then added to the solution with vigorous stirring until the Br_2 color disappeared. The mixture was then transferred to a separatory funnel, and the organic layer was extracted and washed sequentially with brine (20 mL). Thereafter, the organic layer was dried over $MgSO_4$. Then charcoal and Celite were added and stirred for 10 min. The black mixture was filtered to give a clear, colorless liquid. Most solvent was removed by rotary evaporation, and the resulting solid was redissolved in a minimal amount of THF and slowly poured into cold, well-stirred methanol (100 mL) to fully precipitate the product, which was recovered from filtration and dried under vacuum to give a 60% yield of white product.

General Iodination of Ph_7T_8R' and Ph_7T_7-Trisiloxy.[29] To a dry 250 mL Schlenk flask under N_2 was added 70 mL of a 1 M solution ICl in CH_2Cl_2. The flask was then cooled to −40 °C with a cold bath (50% v/v of ethylene glycol in ethanol). Ph_7T_8R' or Ph_7T_7-trisiloxy (5.0 mmol) was added slowly to the reaction mixture. After that, a vent to a bubbler containing aqueous base was added, and the solution was stirred magnetically at −40 °C for 6.0 h. At this point, 20 g of $Na_2S_2O_5$ and 10 g of Na_2CO_3 were dissolved in 40 mL of water and then added to the solution with vigorous stirring until the ICl color disappeared. The mixture was then transferred to a separatory funnel, and the organic layer was extracted and washed sequentially with brine (20 mL). Thereafter, the organic layer was dried over $MgSO_4$, and charcoal and Celite were added and stirred for 10 min. The black mixture was filtered to give a clear, colorless liquid. Most solvent was removed by rotary evaporation. The resulting was solid redissolved in minimal THF and slowly poured into cold, well-stirred methanol (100 mL) to fully precipitate the product. The product was recovered by filtration and dried under vacuum to give a 80% yield of white product.

General Heck Reaction of Brominated and Iodinated Ph_7T_8R' and Ph_7T_7-Trisiloxy.[23,27] To a dry 100 mL Schlenk flask under N_2 were added brominated or iodinated Ph_7T_8R' or Ph_7T_7-trisiloxy (1.0 mmol), $Pd[P(t\text{-}Bu_3)]_2$ (38.7 mg, 0.08 mmol), and $Pd_2(dba)_3$ (34.6 mg, 0.04 mmol), followed by 30 mL of THF, NCy_2Me (2.8 g, 14.0 mmol), and 4-methyl/cyanostyrene (14.0 mmol). The mixture was stirred magnetically at 70 °C for 24 h and then quenched by filtering through 1 cm Celite, which was washed with THF (5 mL). The solution was then concentrated and precipitated into cold, well-stirred methanol (100 mL) and filtered, and the yellowish solid was redissolved in THF (10 mL). The solution was then filtered again through a 1 cm Celite column to remove remaining Pd particles, concentrated, and reprecipitated into cold methanol (50 mL) to give a crude yellow product.

Removal of Pd Catalyst.[24] To a dry 50 mL Schlenk flask under N_2 were added the above product dissolved in toluene (10 mL) and *N*-acetyl-L-cysteine (0.1 g) dissolved in THF (1 mL). The solution was stirred magnetically overnight at room temperature and then filtered through 1 cm Celite to remove the insoluble Pd−cysteine complex. Most solvent was removed by rotary evaporation, and the resulting solid was redissolved in a minimal amount of THF and slowly poured into cold, well-stirred methanol (50 mL) to fully precipitate the product. The product was then recovered by filtration and dried under vacuum to give a 70% yield of yellowish product. MALDI, GPC, FTIR, and TGA were used to characterize product purity.

Analytical Methods. *Matrix-Assisted Laser Desorption/Ionization Time-of-Flight Spectrometry.* MALDI-TOF was done on a Micromass Tof Spec-2E equipped with a 337 nm nitrogen laser in positive-ion reflectron mode using poly(ethylene glycol) as calibration standard, dithranol as matrix, and $AgNO_3$ as ion source. Samples were prepared by mixing solutions of 5 parts matrix (10 mg/mL in THF), 5 parts sample (1 mg/mL in THF), and 1 part $AgNO_3$ (2.5 mg/mL in THF) and blotting the mixture on the target plate.

Nuclear Magnetic Resonance. All ^1H NMR spectra were collected from samples dissolved in $CDCl_3$ and recorded on a Varian INOVA 400 MHz spectrometer. ^1H NMR spectra were collected at 400 MHz using a spectral width of 6000 Hz, a relaxation delay of 0.5 s, 30K data points, a pulse width of 38°, and TMS (0.00 ppm) as the internal reference.

Thermogravimetric Analyses. TGAs were run on a SDT Q600 simultaneous differential DTA-TGA Instrument (TA Instruments, Inc., New Castle, DE). Samples (15−25 mg) were loaded in alumina pans and ramped at 10 °C/min to 1000 °C under dry air with a flow rate of 60 mL/min.

Gel Permeation Chromatography. GPC analyses were done on a Waters 440 system equipped with Waters Styragel columns (7.8 × 300, HT 0.5, 2, 3, and 4) with RI detection using a Waters refractometer and THF as solvent. The system was calibrated by using polystyrene standards.

Fourier-Transform Infrared Spectroscopy. Diffuse reflectance Fourier transform (DRIFT) spectra were recorded on a Nicolet 6700 Series FTIR spectrometer (Thermo Fisher Scientific, Inc., Madison, WI). Optical grade, random cuttings of KBr (International Crystal Laboratories, Garfield, NJ) were ground, with 1.0 wt % of the sample to be analyzed. For DRIFT analyses, samples were packed

DOI: 10.1021/acs.macromol.9b00699
Macromolecules XXXX, XXX, XXX−XXX

Scheme 1. Synthesis of Stilbene-SQs

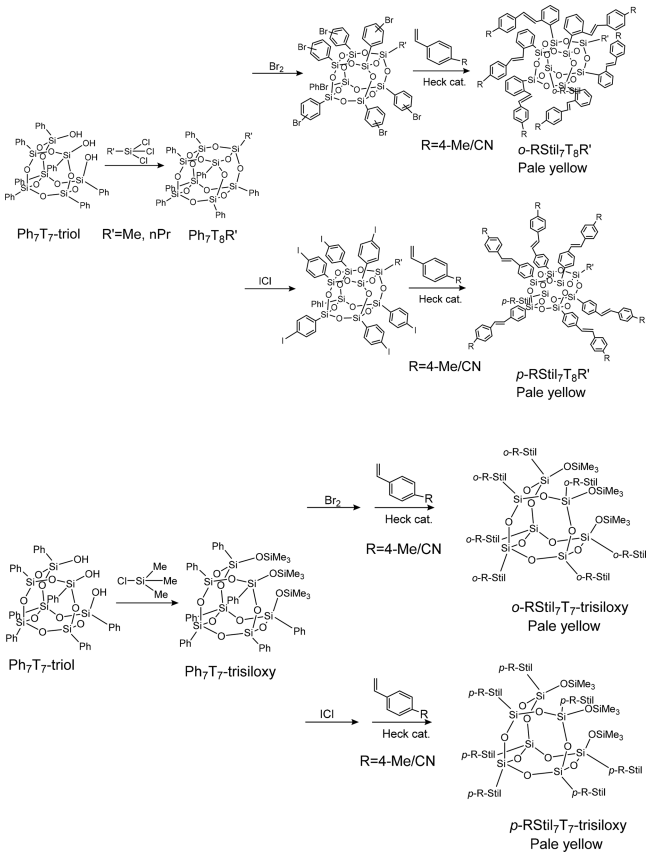

firmly and leveled off at the upper edge to provide a smooth surface. The FTIR sample chamber was flushed continuously with N_2 prior to data acquisition in the range 4000−400 cm^{-1} with a precision of ±4 cm^{-1}.

Photophysical Characterization. *UV−Vis Spectrometry.* UV−vis spectra were recorded on a Shimadzu UV-1601 UV−vis transmission spectrometer. Samples were dissolved in CH_2Cl_2 and diluted to a concentration (10^{-3}−10^{-4} M) where the absorption maximum was <10% for a 1 cm path length.

Photoluminescence Spectrometry. Photoluminescent spectra were recorded on a Fluoromax-2 fluorometer in the required solvent using 300 nm excitation. Samples from UV−vis spectroscopy were diluted (10^{-5}−10^{-6} M) to avoid excimer formation and fluorometer detector saturation.

Two-Photon Studies. *Steady-State Measurements.* All compounds were dissolved in CH_2Cl_2 (Sigma-Aldrich, spectrophotometric grade) for carrying out the optical measurements. The absorption spectra of the molecules were measured using an Agilent (Model No. 8341) spectrophotometer. To measure the molar extinction coefficients, the original stock solutions were diluted to 10^{-6} M. The fluorescence spectra were acquired using a Spex-fluorolog spectrofluorometer. The quantum yields of the molecules were measured using a known procedure.[21] Bis-MSB [*p*-bis(*o*-methylstyryl)benzene] has been used as the standard. The absorbance was limited to less than 0.03. The solutions were purged with argon for 3 min prior to measuring their emission spectra. Then, the following relation was used to measure the quantum yield:[21]

$$\phi_F = (\phi_F)_S \frac{\int J(\bar{\nu})\, d\bar{\nu}}{\int J_S(\bar{\nu})\, d\bar{\nu}} \frac{(J_a)_S}{J_a} \frac{n^2}{n_S^2}$$

where $(\phi_F)_S$ is the quantum yield of the standard, $\int J(\bar{\nu})\, d\bar{\nu}$ the area under the fluorescence emission curve for the sample, $\int J_S(\bar{\nu})\, d\bar{\nu}$ the area under the fluorescence emission curve for the standard $(J_a)_S$ the absorbance of the standard, J_a the absorbance of the sample, n^2 the refractive index of the solvent used for the sample, and n_S^2 the refractive index of the solvent used for the standard.

Two-Photon Excited Fluorescence Measurements. To measure the two-photon absorption cross sections, we followed the two-photon excited fluorescence (TPEF) method.[22] A 10^{-4} M Coumarin 307 (7-ethylamino-6-methyl-4-trifluoromethylcoumarin) solution in methanol was used as the reference for measuring TPA cross sections at different wavelengths. The laser used for the study was a Mai Tai Diode-pumped mode-locked Ti:sapphire laser, which is tunable from 700 to 1000 nm. The beam was directed on to the sample cell (quartz cuvette, 0.5 cm path length), and the resultant fluorescence was collected in a direction perpendicular to the incident beam. A 1 in. focal length plano-convex lens was used to direct the collected fluorescence into a monochromator. The output from the monochromator was coupled to a PMT. The photons were converted into counts by a photon counting unit. A logarithmic plot between collected fluorescence photons and input intensity gave a slope of 2, ensuring a quadratic dependence. The intercept enabled us to calculate the two-photon absorption cross sections at different wavelengths.

Magnetic Scattering Studies.[30−33] Polarization-selective light scattering was investigated in samples excited with 100 fs pulses from an amplified Ti:sapphire laser system operating at 10 kHz repetition rate (amplitude/continuum). SQs were prepared as 0.1 mM solutions in DCM and placed in standard quartz cuvettes to measure light scattering caused by the (nonlinear) magnetoelectric interaction that occurs at the molecular level for intensities in the range 10^8−10^{10} W/cm^2. Complete radiation patterns were recorded for induced electric and magnetic dipole moment strengths in this intensity range by analyzing scattered light to distinguish co-polarized and cross-polarized signal components. By fitting each radiation pattern with a combination of unpolarized and dipolar components versus polar angle, it was possible to compare the librational response determined by the azimuthal potential surface in different SQs.

Computational Methods. Modeling studies were run on ground state geometries were performed using the DFT calculation B3LYP/6-31G(d,p). All of them were performed with a Gaussian 09 program package. To develop an understanding of the asymmetric $T_7(TMS)_3$ molecule, the optimized $T_7(TMS)_3$ structure was first investigated by using local orbitals in a full potential representation, within the framework of density functional theory and the generalized gradient approximation methods as implemented in Gaussian 09. The ground-state geometry was performed by using Becke's three-parameter gradient-corrected exchange potential combined with the Lee−Yang−Parr gradient-corrected correlation potential (B3LYP)[34−36] including Grimme's empirical dispersion correction (DFTD3 with Becke−Johnson damping).[37,38] The 6-31G(d,p) basis set is employed for all atoms.

RESULTS AND DISCUSSION

In previous studies, a set of stilbene-functionalized T_8 compounds were synthesized from $[p\text{-IPhSiO}_{1.5}]_8$ was well as $[o\text{-BrPhSiO}_{1.5}]_8$ using Heck coupling.[19−21] These fully functionalized cages all show UV−vis absorption spectra identical to the spectrum of *trans*-stilbene, while the emission spectra of the full cages show red-shifts of 60−100 nm.[19−21] These large red-shifts are proposed to result from interactions of the stilbene π^* orbitals with a LUMO centered within the cage that has 3-D orbital symmetry, indicating all stilbene moieties interact in the excited state.[19] Such photophysical behavior has been reported previously as indicative of semiconducting-like behavior.[19−21]

Here we demonstrate similar behavior where only monoalkylheptaphenyl or corner missing partial cages are used. In the following section, we first characterize the individual macromonomers synthesized per the Experimental Section; thereafter, we present the photophysical data, and

DOI: 10.1021/acs.macromol.9b00699
Macromolecules XXXX, XXX, XXX−XXX

then the theoretical modeling results as a prelude to discussions about the interpretation of this photophysical data.

Synthesis and Characterization of RStil$_x$T$_8$R′ and RStil$_x$T$_7$-Trisiloxy. In previous studies, we discovered a synthetic route to *o*-Br$_8$OPS with ≥85% ortho-substitution[27] and *p*-I$_8$OPS with >99% monoiodination and >95% para-substitution,[29] and a series of *o*-Br$_x$OPS and *p*-I$_x$OPS were synthesized, which were used as the starting material for the synthesis, via Heck coupling, of a series of stilbene derivatives.[19−21]

Here, we extend our efforts synthesizing a series of alkylphenyl and corner-missing stilbene derivatives from the corresponding brominated and iodinated cages. The first step was to cap the trisilanol corner-missing phenylsilsesquioxane Ph$_7$T$_7$-triol with methyl-/propyltrichlorosilane and trimethylchlorosilane, which give the title closed and corner-missing open cage macromonomers, respectively, as characterized by MALDI-TOF, GPC, and ^{1}H NMR as listed in Table S1. These derivatives were characterized by MALDI-TOF (Figures S1−S12), TGA (Figures S13−S16), GPC, and ^{1}H NMR as listed in Tables S2 and S3.

^{1}H NMR of Br$_x$Ph$_7$T$_8$R in Table S2 shows four signals in the aromatic region. Those of I$_x$Ph$_7$T$_8$R show only two signals, indicating ortho bromination and para iodination as seen previously.

The MALDI-TOF of brominated cages presented in Figures S1 and S4 reveals only traces of dibrominated phenyls. Their TGA ceramic yields (to SiO_2) are close to theory, while MALDI-TOF of iodinated cages presented in Figures S7 and S10 do not show any peaks for diiodophenyl products. The MALDI-TOF data in Table S3 indicate that the substitution patterns of the Heck products are identical to those found for both the brominated and iodinated starting cages without cage breakdown during Heck coupling. Likewise, the TGA ceramic yields of the stilbene derivatives in Table S3 are also close to theory, strongly suggesting quantitative conversion. Decomposition onset temperatures ($T_{d5\%}$/TGA/air) for most Heck products are >400 °C, suggesting high thermal stability arising from the silica-like core. GPC suggests cage sizes grow slightly with Heck coupling by comparing the retention times of the Heck products with starting brominated or iodinated cages. The molecular masses indicated by GPC are not accurate due to the spherical structure of cages, and the retention times for all cage compounds are around 32 min.

We also purposely synthesized the 4-methylstilbene derivative from *p*-I$_8$OPS for comparison for reasons discussed in the following section.

Photophysical Properties. *UV−Vis Studies for o-RStil$_x$T$_8$R′.* Figure 5 provides steady-state spectra (CH_2Cl_2) for *p*-MeStil$_8$OPS synthesized from I$_8$OPS and *o*-RStil$_x$T$_8$R′. The spectra for *o*-MeStil$_x$T$_8$R′ are very similar to those for *p*-MeStil$_8$OPS. As indicated by previous studies as well as results shown here, their UV−vis spectra are all red-shifted 5−10 nm from those of *p*-methylstilbene and the model compound MeStilSi(OEt)$_3$. Normally, it would be reasonable to argue that the effect of the cage on the UV−vis spectra of the attached stilbenes is small. However, it has been suggested in the literature that the −Si(O)$_3$ unit exhibits the inductive characteristics of a −CF$_3$ group.[22] Thus, a blue-shift would be a more reasonable expectation. In contrast to the mundane UV−vis absorption behavior, the emissive behavior is quite striking. As seen in Figure 5, the emission spectra (normalized) show a red-shift of 50−70 nm for all compounds relative to those of *p*-methylstilbene itself, indicating 3-D conjugation in the excited state.[21]

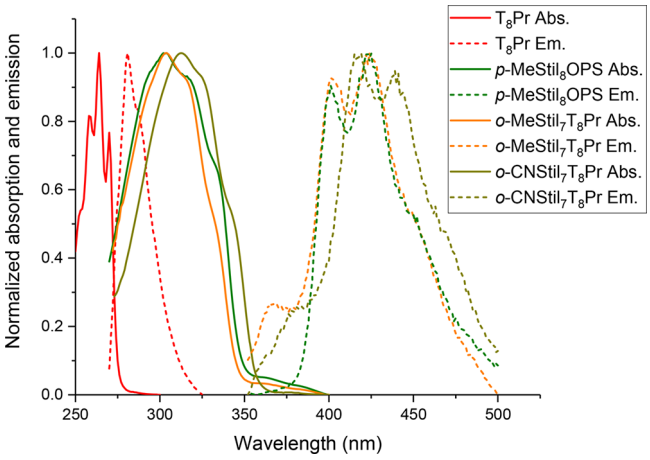

Figure 5. Normalized steady-state spectra for Ph$_7$T$_8$R′, *p*-MeStil$_8$OPS and *o*-RStil$_x$T$_8$R′.

The pair of compounds having structural differences only as a result of a methyl/propyl group show the same spectra, suggesting their optical properties are independent of the nonconjugated side group. The *o*-CNStil$_x$T$_8$R′ compounds display spectra similar to *o*-MeStil$_x$T$_8$R′ but slightly red-shifted ascribed to increased conjugation to the cyano group. The high degree of similarity for the *p*-MeStil$_8$OPS and *o*-MeStil$_x$T$_8$R′ spectra suggest formation of 3-D conjugation even with functionalized heptaphenyl cages.

The TPA data (Table 1) indicate that despite the introduction of an unfunctionalized corner, there are no gross changes in the values recorded, indicating only modest polarization of the individual stilbene groups as expected since the model stilbenes are not capable of charge-transfer-like behavior as seen previously.[19−21]

We have included the TPA data for the highest reported values for cage macromonomers or SQs in our previous studies. These compounds have a strong charge-transfer (CT) component such that in the excited state a large CT transition is observed, reflecting extensive molecular polarization leading to the very large TPA values per group. Coincidentally the Φ_F for these compounds are quite low (0.06/0.07) as expected for CT states.

UV−Vis Data for o/p-RStil$_x$T$_7$-Trisiloxy. Figure 6 provides UV−vis absorption and emission spectra for *p*-MeStil$_8$OPS and *o*-RStil$_x$T$_7$-trisiloxy. Ignoring for the moment the data from *p*-MeStil$_2$Ph$_5$T$_7$-trisiloxy, their spectra are very similar, and all are 5−10 nm red-shifted in absorption and 50−70 nm in emission from *p*-methylstilbene and the model compound MeStilSi(OEt)$_3$, also indicating the existence of 3-D conjugation *even when a corner is missing*. *o*-RStil$_x$T$_7$-trisiloxy shows longer wavelength absorption up to 400 nm, which may arise from the presence of small amounts of dibromophenyl functionality, leading to small amounts of distyrenylbenzene in these SQs. Such longer wavelength absorption was absent in spectra of *p*-MeStil$_8$OPS due to absence of the diiodophenyl functionality and *p*-MeStil$_2$Ph$_5$T$_7$-trisiloxy.

TPA-δ of *o*-MeStil$_7$T$_7$-trisiloxy is only slightly different from other functionalized cage compounds while the TPA-δ of *o*-CNStil$_7$T$_7$-trisiloxy is larger due to the presence of a small amount of dibromophenyl functionality as well as increased conjugation of the cyano group compared to the methyl group.

DOI: 10.1021/acs.macromol.9b00699
Macromolecules XXXX, XXX, XXX−XXX

Table 1. Photophysical Data for *p*-MeStil$_8$OPS, RStil$_x$T$_8$R′, and RStil$_x$T$_7$-Trisiloxy

	Abs λ_{max} (nm)	Em λ_{max} (nm)	E_{Stokes} (cm^{-1})	Φ_F	TPA-δ (GM)
p-MeStilbene[9]	298, 311	355			
MeStilSi(OEt)$_3$[6]	298	352			
[*p*-NH$_2$StilvinylSiO$_{1.5}$]$_8$[19]	361	481	6911	0.06	110
[*p*-NH$_2$StilSiO$_{1.5}$]$_8$[20]	356	459	6303	0.07	26
p-MeStil$_8$OPS[10]	305, 320	400, 422	9142	0.57	0.17
o-MeStil$_6$T$_8$Me	304, 320	402, 426	9530	0.16	1.2
o-MeStil$_7$T$_8$Pr	306, 320	402, 426	9420	0.13	0.9
o-CNStil$_6$T$_8$Me	315, 325	419, 441	8185	0.15	2.0
o-CNStil$_7$T$_8$Pr	315, 325	419, 441	8185	0.19	1.4
p-MeStil$_7$T$_8$Me	305, 317	398, 420	7661	0.17	0.1
p-MeStil$_7$T$_8$Pr	305, 317	398, 421	7661	0.20	0.1
p-CNStil$_7$T$_8$Me	317, 326	415, 442	6578	0.09	2.3
p-CNStil$_7$T$_8$Pr	314, 326	412, 440	6403	0.06	2.8
o-MeStil$_7$T$_7$-trisiloxy	304, 317	406, 418	7793	0.66	0.88
o-CNStil$_7$T$_7$-trisiloxy	314, 326	422, 438	8101	0.42	5.54
p-MeStil$_2$Ph$_5$T$_7$-trisiloxy	299, 311	354	5196	0.73	0.05

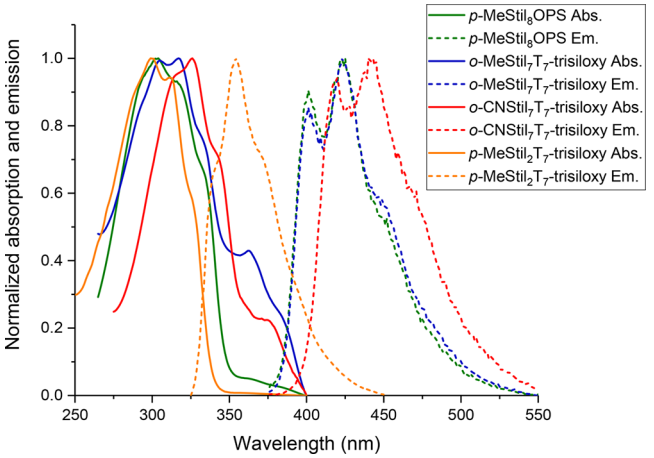

Figure 6. Normalized steady-state spectra for *p*-MeStil$_8$OPS and *o*/*p*-RStil$_x$T$_7$-trisiloxy.

These values contrast greatly with the surprising Φ_F values for the corner-missing cage which are higher to much higher than for complete cages. The reason for this is not clear, but perhaps the bulky trimethylsiloxy (TMS) groups prevent radiationless decay by shielding the cage-centered excited state from solvent collisions that might serve to promote thermal emission from the excited state—hence radiationless decay.

Most telling of all the Table 1 photophysics data reported is that for *p*-MeStil$_2$Ph$_5$T$_7$-trisiloxy. For the first time, we find a stilbene cage that does not show a red-shift in emission. Instead, the absorption and emission are identical to *p*-methylstilbene. Indeed, there is not even a blue-shift in absorption as might be anticipated based on arguments presented above. This molecule does not have a cage-centered LUMO. This is extremely important because it means that these LUMOs can only form at certain degrees of conjugation. That is there is a point where sufficient numbers of conjugated groups must be attached for the LUMO to form inside the cage; otherwise, it is likely phenyl- or stilbene-centered.

The interpretation is that there are clearly structure—property relationships that must be satisfied for 3-D delocalization to occur. This is a valuable discovery because it suggests that there are opportunities to probe, tailor, and optimize properties for applications ranging from high efficiency luminescent components for OLED and white light applications and/or for hybrid photovoltaics, especially if the HOMO LUMO gap can be manipulated. We will in fact demonstrate some ability to do this in a later paper.

Optical Magnetization Properties. Recently, high-frequency magnetization has been induced by intense laser light in a wide variety of materials including simple chemical compounds.[39−42] Nonlinear scattering experiments can characterize 3-D silsesquioxane structures in a novel way that exploits their susceptibility to the joint forces of magnetic and electric optical fields. Magnetoelectric scattering at the molecular level is sensitive to the potential energy surface V within each molecule. This follows from the fact that the slope of the potential determines the azimuthal restoring force of electrons set in motion by the two-photon interaction.[32] This restoring force determines the natural frequency ω_ϕ of oscillations in a torsion pendulum model of the motion[33] as well as the intensity of nonlinear scattering by components of various polarizations. Using a linearized approximation to the slope in a direction perpendicular to the radius of the molecule near the equilibrium point, the natural frequency is expressible as

$$\omega_\phi \simeq \frac{b}{\sqrt{I}}(\mathrm{d}V/\mathrm{d}\phi)_{ave}$$

Here b is a constant that depends on incident light intensity and detuning, and I is the molecular moment of inertia. Small values of ω_ϕ correspond to a nearly flat potential, and large values indicate a steep local potential. It is important to note that ω_ϕ also equals the two-photon detuning denominator for the nonlinear scattering process observed in our experiments. It is for this reason that ω_ϕ is the chief factor determining the relative intensities of polarized or unpolarized scattering channels in the optical interaction.[32] By analyzing ratios of polarized to unpolarized magnetoelectric scattering in different molecules under constant experimental conditions, we can therefore compare the libration frequencies and relative sphericity of their orbitals. To this end, co- and cross-polarized scattered light intensities were recorded and analyzed to distinguish signals of electric and magnetic origin. Then, the comparative sphericity of the excited electron orbitals was determined from the ratio of unpolarized to polarized magnetic signal intensity.

DOI: 10.1021/acs.macromol.9b00699
Macromolecules XXXX, XXX, XXX−XXX

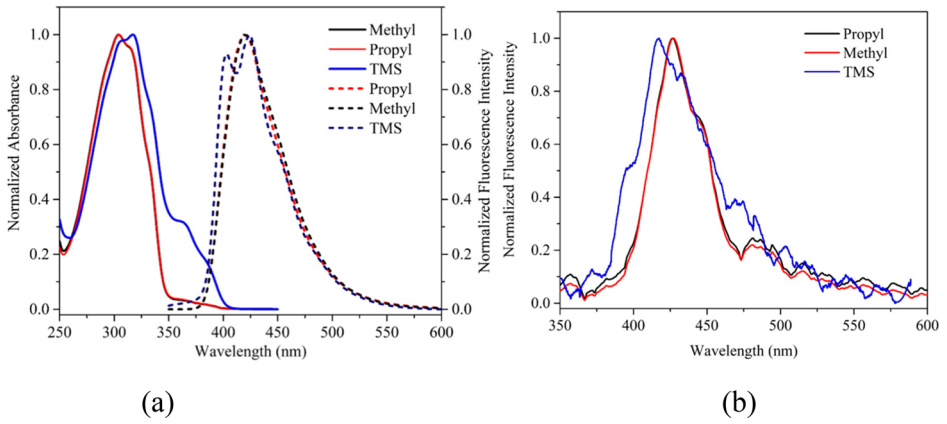

Figure 7. Normalized steady-state one-photon (a) and two-photon (b) fluorescence spectra (λ_{ex} = 800 nm laser light) for *o*-RStil$_7$T$_8$R′ and *o*-RStil$_7$T$_7$-trisiloxy.

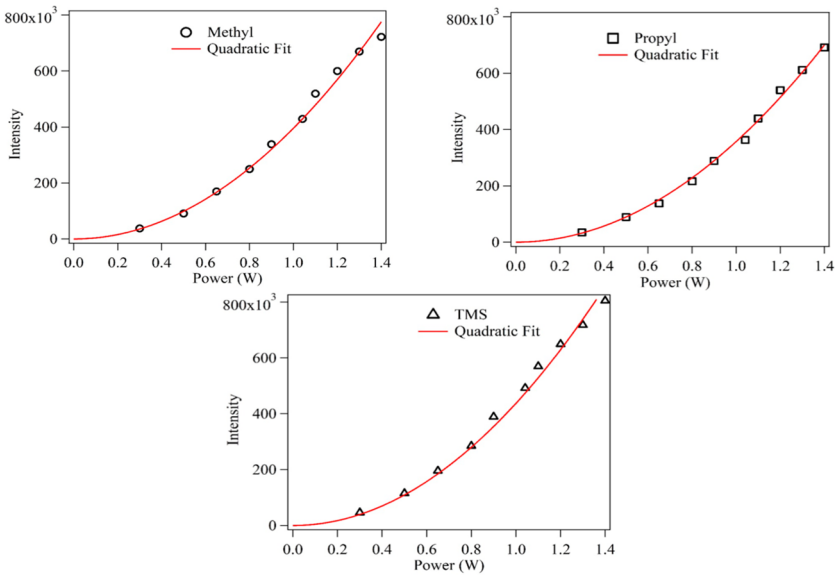

Figure 8. Dependence of two-photon-induced fluorescence emission intensity on input power at λ_{ex} = 800 nm in three different SQ samples: (a) methyl, (b) propyl, and (c) TMS.

For this portion of the characterization, a separate set of absorption and emission spectra were obtained, as shown in Figure 7. The laser wavelength was fixed at 800 nm, so multiphoton absorption was required to cause excitation of fluorescence. Both two- and three-photon absorption processes overlap the electronic transition centered on 320 nm in Figure 7a (at 400 and 267 nm, respectively). Two-photon absorption dominated the excitation, however, in view of the close fit of quadratic intensity dependence to the observed fluorescence intensity in all three SQ samples (Figure 8). Impurities can also participate in two-photon absorption at 400 nm, since this wavelength is relatively far off resonance with the transition to the excited state of the SQ. This was presumed to account for the spectral features of the emission spectrum in the range 475−600 nm that are absent from the one-photon-excited spectrum (Figure 7a,b).

To perform magnetic characterization of SQ samples, we measured the co- and cross-polarized scattered light intensity at 90° to an input beam consisting of 100 fs pulses of various intensities at a wavelength of 800 nm. This type of experiment reveals the relative strength of induced magnetic dipole (MD) scattering in our samples, which is sensitive to azimuthal variations of the electron potential rather than radial variations.

To identify and interpret the theoretical contributions to measured light scattering, we mapped out complete radiation patterns for all samples at fixed input intensity (Figures 9−11). To accomplish this, the analyzer in the detection arm was held in a fixed orientation that either transmitted (red curve) or blocked (blue curve) Rayleigh scattering while the input polarization was rotated through 360°. In Figures 9−12, the component in red is therefore linear electric dipole scattering. The component in blue is nonlinear, cross-polarized scattering of magnetoelectric origin. Note that the (red) electric dipole scattering and the (blue) magnetic dipole scattering share a common unpolarized background, circular in the polar plot, which is also due to magnetoelectric scattering.[32] When analyzed in detail, two separate components are found to be present in each and every recorded polar radiation patterns. One has a purely dipolar ($\cos^2\theta$) variation with angle and is therefore polarized. The other has no dependence on angle and yields an unpolarized, constant background. In the case of cross-polarized scattered light, both components are of magnetic origin.[32] The polarized component in MD scattering

DOI: 10.1021/acs.macromol.9b00699
Macromolecules XXXX, XXX, XXX−XXX

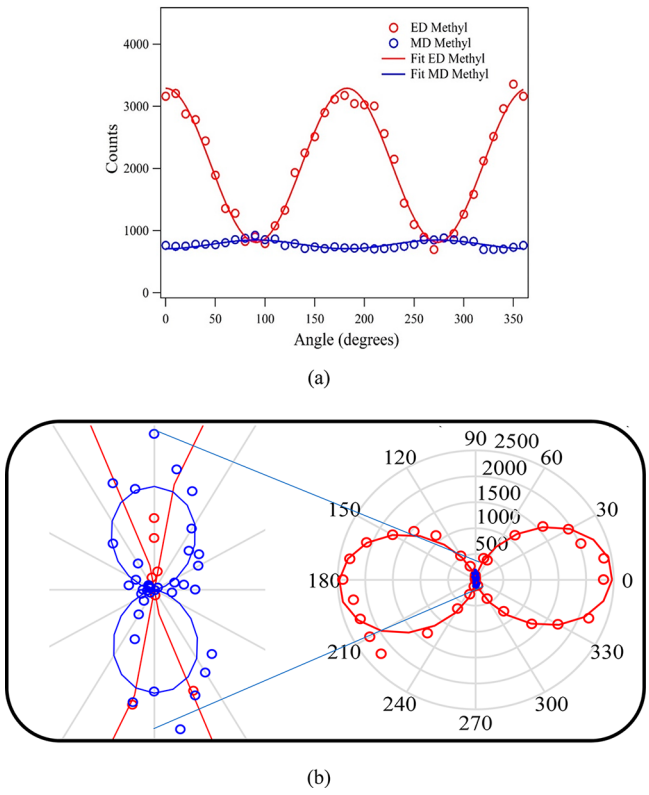

Figure 9. (a) Raw data on co-polarized (red) and cross-polarized (blue) scattered light intensity versus incident polarization angle in 0.1 mM *o*-MeStil$_7$T$_8$Me in DCM at fixed input intensity (λ_{ex}= 800 nm). (b) Radiation pattern (polar plot) of the raw data in part (a) after subtraction of the constant background component, showing that purely dipolar electric and magnetic dipole components are induced in the scattered light at the intensity of our experiments.

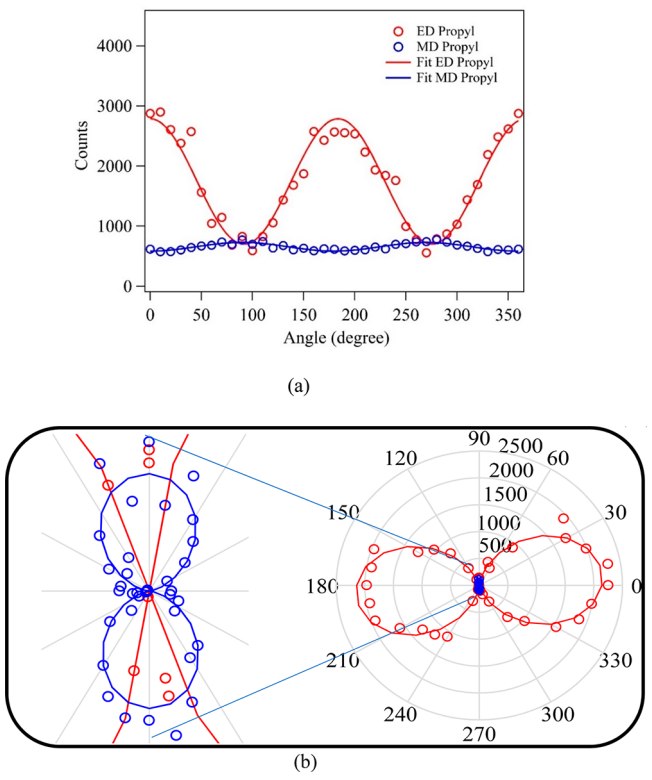

Figure 10. (a) Raw data on co-polarized (red) and cross-polarized (blue) scattered light intensity versus incident polarization angle in *o*-MeStil$_7$T$_8$Pr at fixed input intensity (λ_{ex} = 800 nm). (b) Radiation pattern (polar plot) of the raw data in part (a) after subtraction of the constant background component, showing that purely dipolar electric and magnetic dipole components are induced in the scattered light at the intensity of our experiments.

is a little larger in TMS than in the methyl or propyl variants (Figures 11 and 12). An increase of polarized MD intensity in TMS over that observed in the other samples, measured by the ratio of the angular excursion of scattering intensity over the constant background level in the data, can be interpreted as the result of a deformation in the potential well of the caged electron density. This is discussed next.

In Figures 9−12 the observed scattered light intensities in part (a) of each figure indicate that the magnetic scattering component (blue) has a magnitude that is only 3−5 times smaller than the Rayleigh component (red). Such an intense magnetic component is not observed in linear scattering but arises here due to nonlinear scattering of magnetoelectric origin at the molecular level. What is most significant is the observation that the magnetic component is almost completely unpolarized. For the relatively long duration and small bandwidth of the pulses used in the present experiments, this can only take place if the natural frequency of librations initiated by the magnetic field is extremely low.

The theoretical importance of libration frequency in MD scattering has been discussed previously.[32,33] Unpolarized (blue) MD scattering arises from electrons that are excited by the magnetic force of incident light to undergo azimuthal librations in the local potential well. Their response is governed by the detuning of the optical interaction, which has been shown to equal the resonant libration frequency. If electrons occupy a spherically symmetric orbital whose azimuthal slope is near zero, there is little restoring force. The corresponding libration frequency is therefore low, leading to enhancement of magnetic scattering generally and of unpolarized scattering in particular. On the other hand, if the orbital becomes less spherical through deformation, the libration frequency increases and the unpolarized magnetic scattering intensity is predicted to drop for a fixed pulse duration.

Hence, the comparative sphericity of the excited state orbital can be assessed from the ratio of polarized to unpolarized MD scattering intensities. The lowest ratio corresponds to the most spherically symmetric orbital. If MD scattering is almost completely unpolarized, one can conclude that the excited orbital occupied by the electrons is *spherically symmetric with a near-zero azimuthal slope*. Increasing ratios are indicative of a progressive loss of spherical symmetry. To draw conclusions from experimental data, however, it is important that the electric and magnetic scattering components can be accurately distinguished and that no unexpected components are present from processes that are not magnetoelectric in origin. The accuracy of the separation of components was therefore checked in parts (b) of Figures 9−12. These figures plot the measured radiation patterns for co-polarized ED scattering after subtraction of the unpolarized magnetic background. It is readily apparent that the resultant patterns are purely dipolar in character. Because the residuals are low, one may conclude that only Rayleigh scattering and magnetoelectric scattering contribute significantly to the observed radiation patterns.

DOI: 10.1021/acs.macromol.9b00699
Macromolecules XXXX, XXX, XXX−XXX

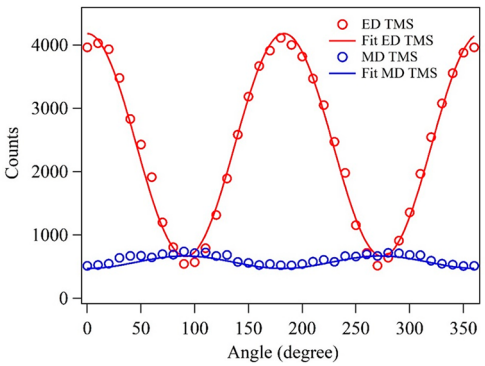

(a)

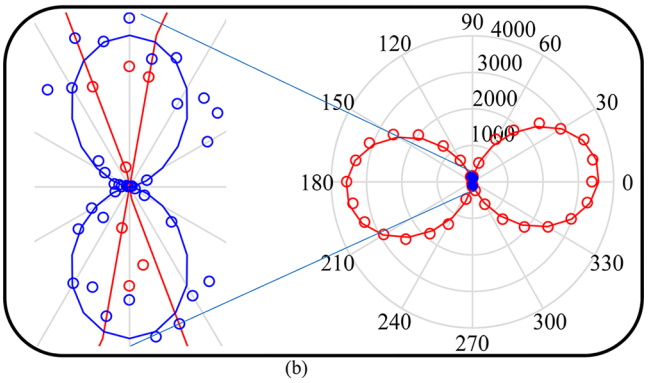

(b)

Figure 11. (a) Raw data on co-polarized (red) and cross-polarized (blue) scattered light intensity versus incident polarization angle in *o*-MeStil$_7$T$_7$-trisiloxyat fixed input intensity (λ_{ex} = 800 nm). (b) Radiation pattern (polar plot) of the raw data in part (a) after subtraction of the constant background component, showing that purely dipolar electric and magnetic dipole components are induced in the scattered light at the intensity of our experiments.

Some basic trends from these studies can be identified. For example, the two-photon fluorescence intensity (two-photon fluorescence quantum yield) is maximum for TMS and minimum for propyl at the same concentrations and conditions in DCM solvent, with methyl being in between the two limits. The MD unpolarized component decreases in the order

$$\text{methyl}_{\text{unpol,MD}} > \text{propyl}_{\text{unpol,MD}} > \text{TMS}_{\text{unpol,MD}}$$

The MD polarized component decreases in the order

$$\text{TMS}_{\text{pol,MD}} > \text{propyl}_{\text{pol,MD}} > \text{methyl}_{\text{pol,MD}}$$

The ED polarized component follows the trend as

$$\text{TMS}_{\text{pol,ED}} > \text{methyl}_{\text{pol,ED}} > \text{propyl}_{\text{pol,ED}}$$

These trends may be interpreted with the help of quantum theory of magnetoelectric interactions on the atomic scale.[32] First, it may be noted that the progression of unpolarized MD intensity is opposite that of the polarized intensities. Theoretically the proportion of these two components is determined by the magnitude of the librational resonance frequency ω_ϕ of electrons responding to incident light. This is due to the fact that the two-photon detuning of the optical excitation equals ω_ϕ when the bandwidth $\Delta\nu$ of the incident light is small ($\Delta\nu < \omega_\phi$). Presuming the active electron density occupies the orbital centered in the cage, the trend is consistent with resonance frequencies in the order

$$\omega_\phi(\text{TMS}) > \omega_\phi(\text{propyl}) > \omega_\phi(\text{methyl})$$

This ordering is justified by the conclusion that the unpolarized scattering channel experiences resonant enhancement as the librational resonance frequency ω_ϕ decreases. The intensity of magnetic scattering should also be proportional to the polarized Rayleigh or ED component, provided the character of the orbital does not change appreciably from one compound to another. This trend is upheld in a comparison of the data for methyl and propyl which differ only in the substituent outside the cage. However, the MD component in the TMS data is reduced in intensity despite a sizable increase in its Rayleigh component as compared to the other two compounds. This is most obvious in Figure 12 where TMS clearly exhibits the largest polarized ED and the smallest unpolarized MD signal components.

As discussed earlier, it is the slope of the orbital potential function that determines the librational resonance frequency. A spherical or nearly spherical potential has a slope close to zero and consequently a low libration frequency which promotes unpolarized MD scattering. Hence, one interpretation of the trends in the data is that they are consistent with the idea *that removing a corner of the cage in the TMS compound distorts the sphericity of the electron orbital in the cage*. It is quite reasonable to expect that the electron potential develops an axis passing through the corner from the cage center. The introduction of this axis could be argued to lead to an increase in the ED transition moment accompanied by an anisotropy of the potential which raises the librational frequency and diminishes the magnetic scattering intensity, consistent with the data. Thus, the magnetic scattering suggests there is a reduction in the sphericity of the LUMO in the cage when a corner is opened but that the effect is relatively subtle.

Modeling Studies. Many recent theoretical studies describe HOMO−LUMO interactions in a wide variety of SQ macromonomers.[43−48] As a prelude to understanding the behavior of the corner-missing cage, we first did calculations for the permethyl cage as shown in Figure 13. The presence of a spherical LUMO that matches very closely those we have reported previously supports the existence of a similar LUMO in the Ph$_7$T$_8$R′ cages described above.

To understand the electronic properties of the Stil$_x$T$_7$-trisiloxy compounds, we calculated the HOMO−LUMO structures of the simplified Me$_7$T$_7$-trisiloxy analogue per Figure 14. From our results for Me$_7$T$_7$-trisiloxy molecule, the HOMO and LUMO energies are −7.37 and 0.91 eV, respectively; a gap of 8.34 eV similar to the theoretical model obtained by Shen et al.[47]

The LUMOs are again localized predominantly in the cage center. *However, the LUMO appears to be asymmetric within the cage in keeping with the photomagnetic studies described above.*

CONCLUSIONS

The above results offer a new perspective on the ease of formation of LUMOs in nonsymmetrical and even incomplete phenyl SQs. They point to the idea that their formation may be of a more general nature than originally suspected. However, the absence of a red-shift for the disubstituted corner-missing SQ with only two methylstilbene moieties indicates there is a threshold for formation of a LUMO inside the cage. This means there are some mitigating electronic effects that control energy levels in and on the cage pointing to the potential for systems where this effect may be tuned through some outside

DOI: 10.1021/acs.macromol.9b00699
Macromolecules XXXX, XXX, XXX−XXX

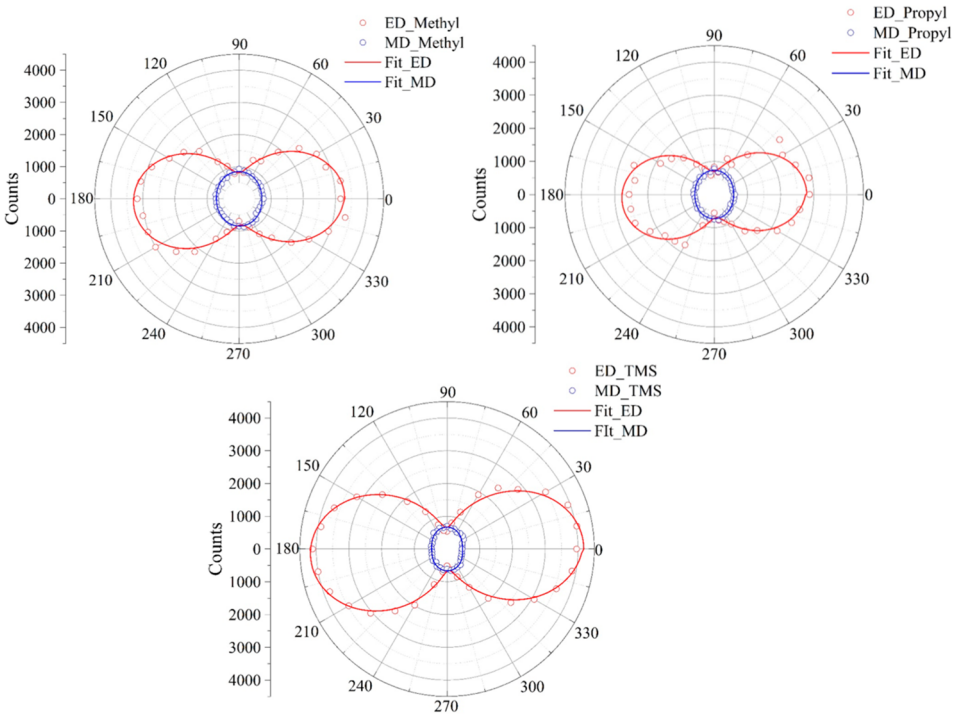

Figure 12. Polar plots of raw light scattering data in methyl, propyl, and TMS monomers after solvent subtraction. The solid curves are least-squares fits to dipole radiation patterns together with a fitted constant background signal.

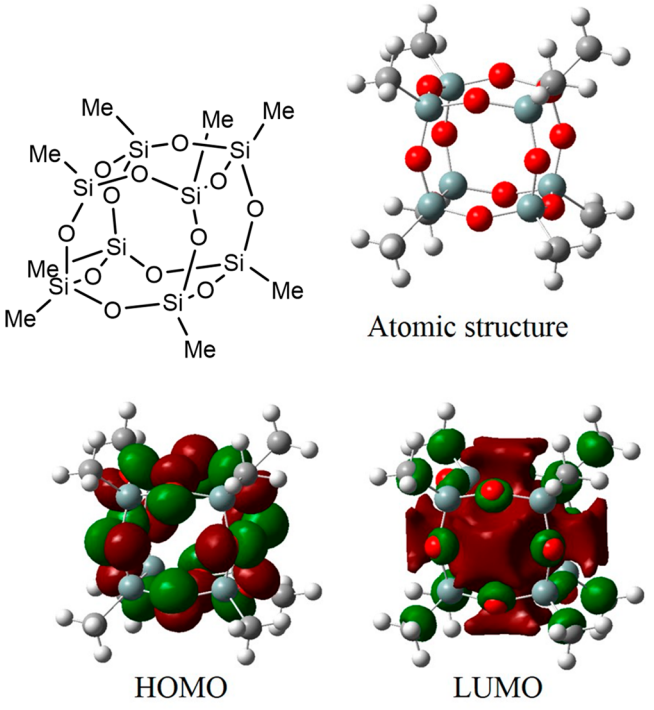

Figure 13. HOMO and LUMO modeling of the Me_8T_8 silsesquioxane.

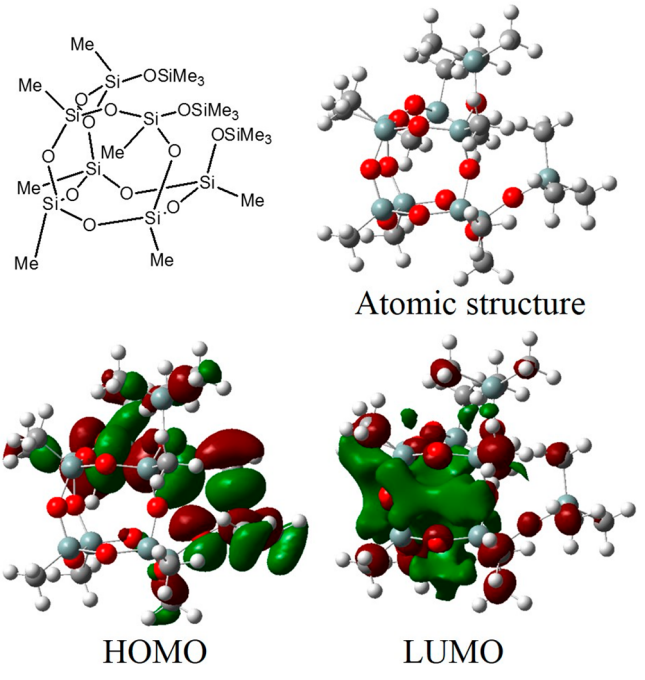

Figure 14. HOMO and LUMO models for the permethylated corner missing cage.

681 stimulus. These results also set the stage for our efforts to look
682 at double-decker cages wherein for example two edges are
683 open yet we still see LUMOs form inside the cage (to be
684 submitted at a later date).
685 Furthermore, we also find that probing magnetoelectric
686 properties using intense laser light provides a new method of
687 confirming not only band gap energies but also LUMO
688 structures and symmetries. We expect to develop this approach
689 to characterization in future papers.
690 The continuing important point to make is that the existence
691 of 3-D conjugation in the excited state points to electronic
692 communication in three dimensions between conjugated
693 moieties that potentially offers access to a wide variety of
694 semiconducting compounds.

DOI: 10.1021/acs.macromol.9b00699
Macromolecules XXXX, XXX, XXX−XXX

■ ASSOCIATED CONTENT

Supporting Information

The Supporting Information is available free of charge on the ACS Publications website at DOI: 10.1021/acs.macromol.9b00699.

Characterization results of silsesquioxane compounds synthesized including MALDI-TOF, ^{1}H NMR, GPC, and TGA (PDF)

■ AUTHOR INFORMATION

Corresponding Author

*E-mail talsdad@umich.edu.

ORCID

Theodore Goodson, III: 0000-0003-2453-2290

Notes

The authors declare no competing financial interest.

■ ACKNOWLEDGMENTS

We thank NSF for support through Chem. Award No. 1610344. S.C.R. thanks the MURI Center for Dynamic Magneto-optics (AFOSR FA9550-14-1-0040) for support of the magnetic scattering studies. S.J. thanks the Human Resources Development in Science Project Science Achievement Scholarship of Thailand (SAST) for support.

■ REFERENCES

(1) Voronkov, M. G.; Lavrent'yev, V. I. Polyhedral Oligosilsesquioxanes and Their Homo Derivatives. *Top. Curr. Chem.* **1982**, *102*, 199–236.

(2) Baney, R. H.; Itoh, M.; Sakakibara, A.; Suzuki, T. Silsesquioxanes. *Chem. Rev.* **1995**, *95*, 1409–30.

(3) Loy, D. A.; Shea, K. J. Bridged Polysilsesquioxanes. Highly Porous Hybrid Organic-Inorganic Materials. *Chem. Rev.* **1995**, *95*, 1431–42.

(4) Calzaferri, G. Silsesquioxanes. In *Tailor-made Silicon-Oxygen Compounds, from Molecules to Materials*; Corriu, R., Jutzi, P., Eds.; Friedr. Vieweg&SohnmbH: Weisbaden, Germany, 1996; pp 149–169.

(5) Lichtenhan, J. Silsesquioxane-based Polymers. In *Polymeric Materials Encyclopedia*; Salmone, J. C., Ed.; CRC Press: New York, 1996; Vol. *10*, pp 7768–77.

(6) Provatas, A.; Matisons, J. G. Synthesis and Applications of Silsesquioxanes. *Trends Polym. Sci.* **1997**, *5*, 327–33.

(7) Li, G.; Wang, L.; Ni, H.; Pittman, C. U. Polyhedral Oligomeric Silsesquioxane (POSS) Polymers and Copolymers: A Review. *J. Inorg. Organomet. Polym.* **2001**, *11*, 123–151.

(8) Duchateau, R. Incompletely Condensed Silsesquioxanes: Versatile Tools in Developing Silica-Supported Olefin Polymerization Catalysts. *Chem. Rev.* **2002**, *102*, 3525–3542.

(9) Abe, Y.; Gunji, T. Oligo- and polysiloxanes. *Prog. Polym. Sci.* **2004**, *29*, 149–182.

(10) Phillips, S. H.; Haddad, T. S.; Tomczak, S. J. Developments in Nanoscience: Polyhedral oligomericsilsesquioxane (POSS)-polymers. *Curr. Opin. Solid State Mater. Sci.* **2004**, *8*, 21–29.

(11) Kannan, R. Y.; Salacinski, H. J.; Butler, P. E.; Seifalian, A. M. Polyhedral Oligomeric Silsesquioxane Nanocomposites: The Next Generation Material for Biomedical Applications. *Acc. Chem. Res.* **2005**, *38*, 879–884.

(12) Laine, R. M. Nano-building Blocks Based on the $[OSiO_{1.5}]_8$ Silsesquioxanes. *J. Mater. Chem.* **2005**, *15*, 3725–44.

(13) Lickiss, P. D.; Rataboul, F. Fully Condensed Polyhedral Silsesquioxanes: From Synthesis to Application. *Adv. Organomet. Chem.* **2008**, *57*, 1–116.

(14) Chan, K. L.; Sonar, P.; Sellinger, A. Cubic Silsesquioxanes for use in Solution Processableorganic Light Emitting Diodes (OLED). *J. Mater. Chem.* **2009**, *19*, 9103.

(15) Wu, J.; Mather, P. T. POSS Polymers: Physical Properties and Biomaterials Applications. *Polym. Rev.* **2009**, *49*, 25–63.

(16) Cordes, D. B.; Lickiss, P. D.; Rataboul, F. Recent Developments in the Chemistry of Cubic Polyhedral Oligosilsesquioxanes. *Chem. Rev.* **2010**, *110*, 2081–2173.

(17) Laine, R. M.; Roll, M. F. Polyhedral Phenylsilsesquioxanes. *Macromolecules* **2011**, *44*, 1073–1220.

(18) Hartmann-Thomson, C. Applications of Polyhedral Oligomeric Silsesquoixanes. In *Advances in Silicon Science*; Springer Science + Business: New York, 2011.

(19) Sulaiman, S.; Bhaskar, A.; Zhang, J.; Guda, R.; Goodson III, T.; Laine, R. M. Molecules with perfect cubic symmetry as nanobuilding blocks for 3-D assemblies. Elaboration of octavinylsilsesquioxane. Unusual luminescence shifts may indicate extended conjugation involving the silsesquioxane core. *Chem. Mater.* **2008**, *20*, 5563–5573.

(20) Laine, R. M.; Sulaiman, S.; Brick, C.; Roll, M.; Tamaki, R.; Asuncion, M. Z.; Neurock, M.; Filhol, J.-S.; Lee, C.-Y.; Zhang, J.; Goodson, T., III; Ronchi, M.; Pizzotti, M.; Rand, S. C.; Li, Y. Synthesis and photophysical properties of stilbeneoctasilsesquioxanes. Emission behavior coupled with theoretical modeling studies suggest a 3-D excited state involving the silica core. *J. Am. Chem. Soc.* **2010**, *132*, 3708–3722.

(21) Sulaiman, S.; Zhang, J.; Goodson, T., III; Laine, R. M. Synthesis, Characterization and Photophysical Properties of Polyfunctional Phenylsilsesquioxanes: $[o\text{-RPhSiO}_{1.5}]_8$, $[2,5\text{-R}_2\text{PhSiO}_{1.5}]_8$, and $[\text{R}_3\text{PhSiO}_{1.5}]_8$. *J. Mater. Chem.* **2011**, *21*, 11177–11187.

(22) Feher, F.; Budzichowski, T. A. Syntheses of highly-functionalized polyhedral oligosilsesquioxanes. *J. Organomet. Chem.* **1989**, *379*, 33–40.

(23) Bahrami, M.; Hashemi, H.; Ma, X.; Kieffer, J.; Laine, R. M. Why do the $[PhSiO_{1.5}]_{8,10,12}$ cages self-brominate primarily in the ortho position? Modeling reveals a strong cage influence on the mechanism. *Phys. Chem. Chem. Phys.* **2014**, *16*, 25760–25764.

(24) Bahrami, M.; Furgal, J. C.; Hashemi, H.; Ehsani, M.; Jahani, Y.; Goodson, T., III; Kieffer, J.; Laine, R. M. Synthesis and Characterization of Nano-building Blocks $[o\text{-RStyrPhSiO}_{1.5}]_{10,12}$ (R = Me-, MeO-, NBoc- and CN. Unexpected Photophysical Properties Arising from Apparent Asymmetric Cage Functionalization as Supported by Modelling Studies. *J. Phys. Chem. C* **2015**, *119*, 15846–15858.

(25) Moghadam, M.; Kampf, J.; Laine, R. M. Unpublished results.

(26) Ohshita, J.; Tsuchida, T.; Komaguchi, K.; Yamamoto, K.; Adachi, Y.; Ooyama, Y.; Harima, Y.; Tanaka, K. Studies on Spherically Distributed LUMO and Electron-Accepting Properties of Caged Hexakis(germasesquioxanes). *Organometallics* **2017**, *36*, 2536.

(27) Li, Z.; Kawakami, Y. Formation of incompletely condensed oligosilsesquioxanes by hydrolysis of completely condensed POSS via reshuffling. *Chem. Lett.* **2008**, *37*, 804–805.

(28) Roll, M. F.; Mathur, P.; Takahashi, K.; Kampf, J. W.; Laine, R. M. $[PhSiO_{1.5}]_8$ promotes self-bromination to produce $[o\text{-BrPhSiO}_{1.5}]_8$: further bromination gives crystalline $[2,5\text{-Br}_2\text{PhSiO}_{1.5}]_8$ with a density of 2.32 g cm^{-3} and a calculated refractive index of 1.7 or the tetraicosa bromo compound $[\text{Br}_3\text{PhSiO}_{1.5}]_8$. *J. Mater. Chem.* **2011**, *21*, 11167–11176.

(29) Roll, M.; Asuncion, M. Z.; Kampf, J.; Laine, R. M. *para*-Octaiodophenylsilsesquioxane, $[p\text{-IC}_6\text{H}_4\text{SiO}_{1.5}]_8$, a nearly perfect nanobuilding block. *ACS Nano* **2008**, *2*, 320–6.

(30) Rand, S. C.; Fisher, W. M.; Oliveira, S. L. Optically-induced magnetization in Homogeneous Dielectric Media. *J. Opt. Soc. Am. B* **2008**, *25*, 1106–1117.

(31) Fisher, A. A.; Dreyer, E. F. C.; Chakrabarty, A.; Rand, S. C. Optical Magnetization Part I: Experiments on Radiant Optical Magnetization in Solids. *Opt. Express* **2016**, *24*, 26064–20679.

(32) Fisher, A. A.; Dreyer, E. F. C.; Chakrabarty, A.; Rand, S. C. *Opt. Express* **2016**, *24*, 26055–20663.

DOI: 10.1021/acs.macromol.9b00699
Macromolecules XXXX, XXX, XXX–XXX

(33) Dreyer, E. F. C.; Fisher, A. A.; Smail, G.; Anisimov, P.; Rand, S. C. Optical Magnetization Part III: Theory of Molecular Magneto-electric Rectification. *Opt. Express* **2016**, *24*, 26064−20679.
(34) Vosko, S. H.; Wilk, L.; Nusair, M. ,"Accurate spin-dependent electron liquid correlation energies for local spin density calculations: a critical analysis. *Can. J. Phys.* **1980**, *58*, 1200−1211.
(35) Lee, C.; Yang, W.; Parr, R. G. Development of the Colle-Salvetti correlation-energy formula into a functional of the electron density. *Phys. Rev. B: Condens. Matter Mater. Phys.* **1988**, *37*, 785−789.
(36) Becke, A. D. Density-functional exchange-energy approximation with correct asymptotic behavior. *Phys. Rev. A: At., Mol., Opt. Phys.* **1988**, *38*, 3098−3100.
(37) Grimme, S.; Antony, J.; Ehrlich, S.; Krieg, H. A consistent and accurate *ab initio* parametrization of density functional dispersion correction (DFT-D) for the 94 elements H-Pu. *J. Chem. Phys.* **2010**, *132*, 154104.
(38) Grimme, S.; Ehrlich, S.; Goerigk, L. Effect of the damping function in dispersion corrected density functional theory. *J. Comput. Chem.* **2011**, *32*, 1456−1465.
(39) Anderson, S. E.; Bodzin, D. J.; Haddad, T. S.; Boatz, J. A.; Mabry, J. M.; Mitchell, C.; Bowers, M. T. Structural Investigation of Encapsulated Fluoride in Polyhedral Oligomeric Silsesquioxane Cages Using Ion Mobility Mass Spectrometry and Molecular Mechanics. *Chem. Mater.* **2008**, *20*, 4299−4309.
(40) Azinović, D.; Cai, J.; Eggs, C.; König, H.; Marsmann, H. C.; Vepřek, S. Photoluminescence from silsesquioxanes $R_8(SiO_{1.5})_8$. *J. Lumin.* **2002**, *97*, 40−50.
(41) Chen, Y.; Schneider, K. S.; Banaszak Holl, M. M.; Orr, B. G. Simulated scanning tunneling microscopy images of three-dimensional clusters: H8Si8O12 on Si(100)-2 × 1. *Phys. Rev. B: Condens. Matter Mater. Phys.* **2004**, *70*, 085402.
(42) Li, H.-C.; Lee, C.-Y.; McCabe, C.; Striolo, A.; Neurock, M. Ab Initio Analysis of the Structural Properties of Alkyl-Substituted Polyhedral Oligomeric Silsesquioxanes. *J. Phys. Chem. A* **2007**, *111*, 3577−3584.
(43) Marcolli, C.; Calzaferri, G. Monosubstituted octasilasesquioxanes. *Appl. Organomet. Chem.* **1999**, *13*, 213−218.
(44) McCabe, C.; Glotzer, S. C.; Kieffer, J.; Neurock, M.; Cummings, P. T. Multiscale Simulation of the Synthesis, Assembly and Properties of Nanostructured Organic/Inorganic Hybrid Materials. *J. Comput. Theor. Nanosci.* **2004**, *1*, 265−279.
(45) Ossadnik, C.; et al. Photolumineszenzeigenschaften von substituierten Silsesquioxanen der Zusammensetzung Rn(SiO1.5)n. In *Silicon Chemistry*; Springer: Vienna, 1999; pp 55−68.
(46) Park, S. S.; Xiao, C.; Hagelberg, F.; Hossain, D.; Pittman, C. U.; Saebo, S. Endohedral and Exohedral Complexes of Polyhedral Double Four-Membered-Ring (D4R) Units with Atomic and Ionic Impurities. *J. Phys. Chem. A* **2004**, *108*, 11260−11272.
(47) Shen, J.; Cheng, W.-D.; Wu, D.-S.; Li, X.-D.; Lan, Y.-Z.; Zhang, H.; Gong, Y.-J.; Li, F.-F.; Huang, S.-P. Modeling of configurations and third-order nonlinear optical properties of methyl silsesquioxanes. *J. Chem. Phys.* **2005**, *122*, 204709.
(48) Striolo, A.; McCabe, C.; Cummings, P. T. Thermodynamic and Transport Properties of Polyhedral Oligomeric Silsesquioxanes in Poly(dimethylsiloxane). *J. Phys. Chem. B* **2005**, *109*, 14300−14307.

DOI: 10.1021/acs.macromol.9b00699
Macromolecules XXXX, XXX, XXX−XXX